Copyright © 1991 IEEE

Reprinted from
IEEE journal of quantum electronics 27 (1991), S. 737 - 752

This material is posted here with permission of the IEEE. Such permission of the IEEE does not in any way imply IEEE endorsement of any of Universität Ulm's products or services. Internal or personal use of this material is permitted. However, permission to reprint/republish this material for advertising or promotional purposes or for creating new collective works for resale or redistribution must be obtained from the IEEE by writing to pubs-permissions@ieee.org.

By choosing to view this document, you agree to all provisions of the copyright laws protecting it.

InGaAs Metal–Semiconductor–Metal Photodetectors for Long Wavelength Optical Communications

Julian B. D. Soole and Hermann Schumacher

Abstract—**Interdigitated metal–semiconductor–metal (MSM) Schottky barrier photodetectors based on the InGaAs–InP material system have been the subject of keen research over the past couple of years for use in long wavelength communication systems. This paper reviews the properties of these detectors and discusses the current state-of-the-art performance achieved by experimental devices. The experimental work concentrates on the barrier-enhanced lattice-matched InAlAs–InGaAs device grown by low pressure OMCVD, which has to date yielded detectors with the highest performance characteristics. Current research on their integration with FET's to form monolithic receivers and with waveguides for on-chip optical signal processing is also included.**

I. Introduction

The planar metal–semiconductor–metal (MSM) photodetector is illustrated schematically in Fig. 1. It consists of a semiconductor absorbing layer on which two interdigitated electrodes have been deposited to form back-to-back Schottky diodes. The detector is extremely easy to fabricate. The compatibility of the detector structure with FET's (see Fig. 2), together with the planarity of the contacts, results in a minimal increase of process complexity when the MSM is integrated with MESFET or HEMT circuitry. The electrode deposition stage may generally be combined with other metalizations in the fabrication of an integrated receiver circuit. These combined advantages have lead to its widespread use as a detector front-end in GaAs based integrated receivers [1]–[4]. The most complex integrated GaAs receiver reported to date, employing over 2000 devices in four parallel receiver clock-recovery circuits [4], used GaAs MSM detectors.

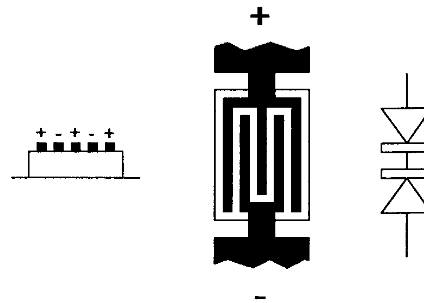

Fig. 1. Schematic diagram of the generic MSM detector. Interdigitated electrodes form Schottky contacts on the absorbing semiconductor, which is usually grown epitaxially often after a buffer layer and may be mesa-etched for isolation.

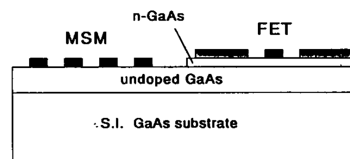

Fig. 2. An example of GaAs MSM–FET integration, showing device compatibility and the ease of integration of the MSM. (After [1]).

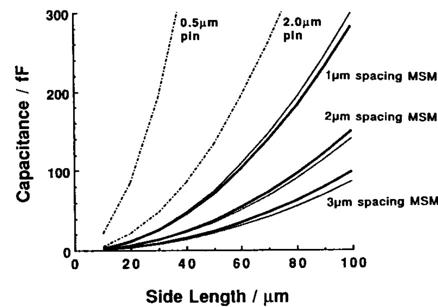

Fig. 3. Capacitance versus edge length of the interdigitated area, for 1, 2, and 3 μm spacing MSM's. The solid lines are for 1 μm wide electrodes, and the dotted lines for 0.5 μm fingers. The capacitance of a p-i-n with 0.5 and 1.0 μm thick semiconductor is also plotted, for comparison.

Aside from its planarity and compatibility with FET's, the interdigitated electrode structure of the planar MSM gives the detector a very low capacitance per unit area. Fig. 3 graphs the capacitance of MSM's with typical device dimensions against the side-length of the interdigitated area. The low capacitance means that a large area MSM, such as might be used with ease with a multimode fiber, may be used in conjunction with a high impedance integrating amplifier without necessarily compromising the bandwidth. Also, as the equivalent input noise current in FET's is proportional to the square of the total front end capacitance, $(C_{\text{detector}} + C_{gs} + C_{\text{stray}})^2$, a low detector capacitance benefits receiver sensitivity [5], [6].

High-performance GaAs MSM's for use in the 0.8 μm wavelength band have proved relatively easy to fabricate [7]–[9] because good-quality high-barrier (~0.7 V) Schottky contacts can be readily obtained on GaAs. Operation at the longer wavelengths of interest to long haul optical fiber communications, 1.3 and 1.55 μm, however, requires the use of the narrow band-gap InGaAs–InP material system. Unfortunately, undoped InGaAs (n^-) has a low Schottky barrier height (~0.2 V [10]).

Manuscript received January 8, 1991.
J. B. D. Soole is with Bellcore, Red Bank, NJ 07701.
H. Schumacher was with Bellcore, Red Bank, NJ 07701. He is now with the University of Ulm, Germany.
IEEE Log Number 9143402.

0018-9197/91/0300-0737$01.00 © 1991 IEEE

Authorized licensed use limited to: IEEE Xplore. Downloaded on March 4, 2009 at 03:08 from IEEE Xplore. Restrictions apply.

This means that direct deposition of the electrode on the InGaAs gives detectors with an unacceptably large leakage current even at low biases. Various schemes have therefore been explored to "enhance" this Schottky barrier and so limit the dark current. Thin strained layers of GaAs [11] and AlGaAs [12, 13], both of which have higher Schottky barriers, have been grown on InGaAs, and dielectric films have been deposited using a Langmuir-Blodgett technique [14]. The device performance in these cases was rather poor, with moderate leakage currents, significant low frequency gain, and pulse responses with long tail portions indicating a significant trap density. Recently InP:Fe, which pins the Fermi level at midgap has also been employed [15], though this too produced devices with a significant pulse response tail and internal gain.

The most promising barrier enhancement technique reported to date has been the growth of a thin layer of undoped lattice-matched InAlAs [16]–[22] on the InGaAs. InAlAs lattice matched to InP ($E_g = 1.47$ V) has a high Schottky barrier of ~ 0.8 V [23] and a thin layer grown epitaxially on InGaAs has the effect of raising both the electron and hole barriers. Both Organo-Metallic Chemical Vapor Deposition (OMCVD) grown [16], [18]–[20] and MBE grown [17], [22] material has yielded devices with good performance characteristics. In the following sections, most of the experimental results reported will be for devices grown by low pressure (76 torr) OMCVD, which is the growth process used by the authors. Provided care is taken to exclude all sources of oxygen from the reactor, low pressure OMCVD is found to give high-quality InAlAs and an InAlAs–InGaAs heterointerface which possesses a low density of defects. Electron beam evaporated Ti–Au was used for the Schottky electrode metal, typically 200 Å Ti followed by 2000 Å of Au. A typical fabricated device is shown in Fig. 4, along with a schematic of the detector cross section.

An alternative approach being pursued by some workers is the growth of $In_xGa_{1-x}As$ on GaAs substrates [24], [25]. In [24], a layer of intermediate lattice constant is interposed between absorbing $In_{0.4}Ga_{0.8}As$ and the substrate in an effort to prevent misfit dislocations from entering the optoelectronically active detector material. Although to date the performance of mismatched InGaAs detectors has been inferior to those of lattice-matched InGaAs–InP devices, this approach holds the potential for coupling into mature GaAs integrated device technology.

In the following sections we shall discuss some of the properties of InGaAs MSM detectors and give experimental results for InAlAs–InGaAs devices grown by low pressure OMCVD. These represent the best performances so far obtained for the InGaAs MSM. First of all, we consider the detector capacitance, which of course depends only on the geometry and the semiconductor dielectric constant and so is generic to the MSM. Then we give the diode I–V characteristics and discuss the form of the dark current. We then consider the CW photoresponse and the matter of internal gain. In Section VI, we examine the noise performance of these lattice-matched devices and in Section VII we consider the temporal performance of the MSM. We give computations of the transit-time limited impulse response, and show how the response speed depends on the different device dimensions, comparing our findings with some experimental results. Section VII concludes with an examination of the trade off which occurs between bandwidth and efficiency. We finish the paper with a look at the present work on integrating the InGaAs MSM with FET's in monolithic photoreceivers, and with semiconductor waveguides for on-chip optical signal processing.

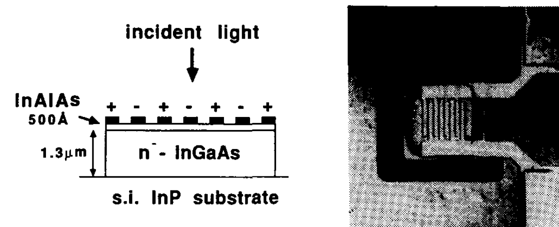

Fig. 4. A typical fabricated detector. The interdigitated electrodes cover the central portion of a 40 × 40 μm etched mesa. A polyimide collar prevents the electrodes contacting the mesa sides and aids edge coverage.

II. Capacitance of the MSM

As outlined above, one of the advantages of the interdigitated MSM is its low capacitance per unit area. Typical photolithographically defined devices have electrode fingers widths of ~ 1 μm and interdigital spacings of 1–3 μm. This electrode structure has a capacitance of just a few $\mathrm{fF}/(10\ \mu\mathrm{m})^2$. For an undoped and infinitely thick semiconductor, the capacitance is given [26] by

$$C = \frac{K(k)}{K(k')} \epsilon_0 (1 + \epsilon_r) \frac{A}{\text{finger period}} \tag{1}$$

where ϵ_r is the relative dielectric constant of the semiconductor, A is the interdigitated area, and $K(\kappa)$ is the complete elliptic integral of the first kind,

$$K(\kappa) = \int_0^{\pi/2} [1/\sqrt{(1 - \kappa^2 \sin^2 \varphi)}\, d\varphi$$

with

$$k = \tan^2 [\pi \text{ (finger width)}/4 \text{ (finger period)}]$$

and

$$k' = \sqrt{(1 - k^2)}.$$

Fig. 3 plots the capacitance derived from this expression as a function of $\sqrt{A}$, for three electrode spacings: 1, 2, and 3 μm. The solid lines are the capacitance for an electrode finger width of 1 μm and the dotted lines are for an electrode width of 0.5 μm—the difference is seen to be only marginal. For comparison, the capacitance of a p–i–n diode with both a 0.5 and a 2.0 μm InGaAs layer is also plotted. It is seen that the capacitance of the MSM is significantly lower than that of the p–i–n, even when comparing the rather thick (2 μm) p–i–n and the narrow spacing (1 μm) MSM. This means that the bandwidth of a receiver incorporating an MSM front end will in general not be limited by the detector capacitance. We also note that there will only be a small addition to the input noise, which is proportional to $(C_{\text{detector}} + C_{gs} + C_{\text{stray}})^2$.

A detector suitable for coupling to a single-mode fiber might have an active area in the region of 50 × 50 μm. An MSM with 1 μm electrodes and a 2 μm spacings—which is typical of the detectors reported to date—will then have a capacitance of ~ 40 fF. This gives an RC charging time of just 1.9 ps into a 50 Ω load. In comparison, the transit times of the photogenerated carriers will be of order [(electrode separation)/2 (saturation velocity)], which is a few tens of ps. The response into 50 Ω is therefore limited by the carrier transit times. This will continue

Authorized licensed use limited to: IEEE Xplore. Downloaded on March 4, 2009 at 03:08 from IEEE Xplore. Restrictions apply.

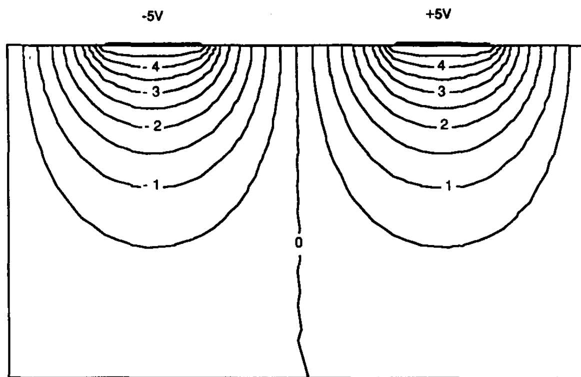

Fig. 5. Potential distribution in a "1 × 2" MSM. The lines are calculated for a 10 V bias using a finite element computer program.

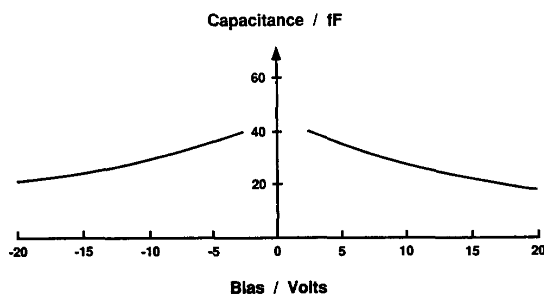

Fig. 6. Capacitance as a function of applied bias for an MSM with 1 μm fingers, 2 μm spacings, and 1 μm thick InGaAs. The residual doping is $\sim 6\ 10^{14}$ cm^{-3}. The slight asymmetry is attributed to the slightly unequal electrode areas in contact with the semiconductor.

to be the case for moderate increases in the load impedance, or alternatively for a moderate increase in the detector area or decrease in the finger spacing. Indeed, it is generally true that for photolithographically defined InGaAs MSM detectors the finite carrier transit times will be the factor which limits the frequency response. Later, in Section VII, we consider how these transit times are governed by the device geometry and what limitation they put on the detector bandwidth.

The above formulation is for an undoped (and semiinfinite) semiconductor. In practice, the InGaAs of the MSM has a residual doping level in the region of 5-10 $\times$ 10^{14} cm^{-3} and a few volts bias is required to deplete a typical device. Once depleted, the capacitance is then given by (1) and the electric field profile is only slightly perturbed from that of the undoped device. The potential distribution in a 1 μm finger, 2 μm spacing, device, "1 × 2", is given in Fig. 5. The extent of the depletion can be estimated from a capacitance/voltage plot, a typical example of which is given in Fig. 6. The trace is for a "1 × 2" detector with a 2 μm thick, $n \sim 6 \times 10^{14}$ cm^{-3}, InGaAs layer. The trace for a device with a thinner InGaAs layer flattens out at lower biases. Unlike a one-dimensional MSM—i.e., one with collinear electrodes and semiconductor (as treated by Sze, [27])—where complete depletion occurs at the "punch-through" bias and the capacitance remains constant thereafter, the interdigitated MSM continues to deplete regions further from the surface, under the electrodes, and beneath the absorption layer, so the capacitance continues to decrease even at quite high biases. It should be noted, however, that for the most part the region of interest is that directly below the interelectrode spacing and not more than 1 μm or so from the surface, and that this region will be effectively depleted at biases less than that required to "bottom-out" the C-V curve. Complete depletion of this region is nevertheless essential if a high internal quantum efficiency and a fast response is to be obtained (see below).

III. Diode Characteristics

As discussed in the introduction, the growth of a thin layer of lattice-matched $In_{0.52}Al_{0.48}As$ on the $In_{0.53}Ga_{0.47}As$ has proved to be the most successful technique for producing low leakage detectors [16]-[20], [22]. The $In_{0.52}Al_{0.48}As$ ($E_g = 1.47$ V) has a high Schottky barrier height of ~ 0.8 V [23] and the thin epitaxial layer has the effect of raising the Schottky barrier on n^--InGaAs, which is only ~ 0.2 V, and limiting the dark current [16]-[22].

The data given below and throughout this article is for $In_{0.52}Al_{0.48}As$-$In_{0.53}Ga_{0.47}As$ detectors grown by low pressure (76 torr) OMCVD. The InAlAs layer so-grown is of high crystalline quality (a low divergence of $<24''$ is obtained for the (004) CuKα diffracted beam with $\Delta a/a \sim 1.1 \times 10^{-3}$) and the InAlAs-InGaAs interface has a low density of traps; a room temperature mobility of 11900 cm^{2}V^{-1}s^{-1} is typically obtained in a modulation doped structure ($n_s = 2.4\ 10^{12}$ cm^{-2}) [16]. The residual InGaAs doping for the devices presented is typically 6-8 $\times$ 10^{14} cm^{-3}, with n^--InAlAs at 5-10 $\times$ 10^{14} cm^{-3}. The Schottky metal is Ti-Au.

The dark I-V characteristic of a typical device is given in Fig. 7. This detector has nominally 1 μm finger widths and 2 μm electrode spacings, and employed an 800 Å InAlAs layer. The leakage current densities are ~ 25 pA/μm^2 at 15 V and <300 pA/μm^2 at 30 V, with a breakdown voltage of 35-40 V. These values are somewhat better than the best previously reported for the InAlAs-InGaAs device [20] and are the lowest leakage figures reported so far for the barrier enhanced InGaAs detector. The full curve is shown in the inset and is symmetrical, as expected. Fig. 7 has the same general form as that found for low leakage GaAs MSM's [8], [28].

The I-V curve in Fig. 7 shows a "knee" at low bias (~ 1 V). This occurs as the anode contact becomes forward biased. For typical detectors, the voltage required is 1-5 V, depending on the electrode spacing and the residual doping level. This knee bias is close to that suggested by a simple one-dimensional model [27], which gives the voltage for flat band at the anode V_{fb} as

$$V_{fb} = (q\,N_d/2\epsilon)L^2 \tag{2}$$

where L is the electrode spacing and N_d is the residual doping level. The current flow in the planar MSM at low biases would occur predominantly in a thin subsurface layer, so this correspondence might be expected. The photoresponse curves, to be discussed in the next section (see Fig. 9), also show a "knee" and a close examination reveals that its position shifts slightly to higher biases as the illumination increases—presumably the result of the increased space charge present.

At biases less than V_{fb}, the dark current is negligible. Just above the flat-band condition, a substantial fraction of the elec-

Authorized licensed use limited to: IEEE Xplore. Downloaded on March 4, 2009 at 03:08 from IEEE Xplore. Restrictions apply.

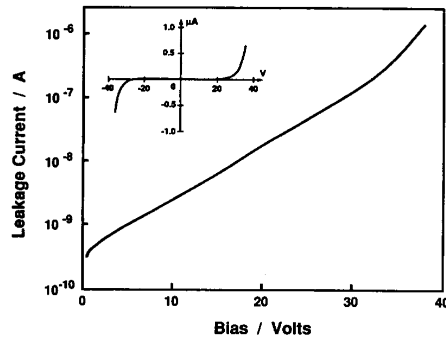

Fig. 7. Dark current of a "1 × 2" device with an electrode contact area of ~350 μm^2 and an 800 Å InAlAs barrier layer. The inset shows the symmetric nature of the characteristic.

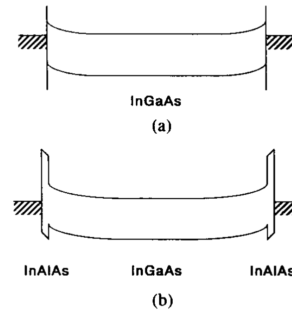

Fig. 8. Band diagrams of the one-dimensional approximation to the planar MSM. (a) The simple Schottky barrier approximation. (b) A more detailed picture of the heteroenhancement layer. For a "thick" InAlAs layer, we expect independent formation of the InAlAs-electrode Schottky barrier and the InGaAs-InAlAs heterojunction.

tron-hole pairs generated may still recombine if the separating field is not strong. Also, the InGaAs furthest from the surface may not be fully depleted. Thus, a somewhat higher applied bias is required before unity quantum efficiency is attained. As seen later, in Section VII, a higher bias is also required to obtain a fast detector response.

The general form of the I-V curve shown in Fig. 7 is similar to that expected for a simple one-dimensional back-to-back Schottky diode [27]. Qualitatively, this similarity is to be expected. However, the planar MSM differs from the one-dimensional device in two distinct ways. First, the detector is two-dimensional and the field lines are nonparallel. This leads to nonuniform conduction that can only be approximated by a one-dimensional formalism. Second, the electrode interface is by no means a "simple" Schottky contact. Although the InAlAs has to date been simply regarded as a means of raising the effective Schottky barrier on the InGaAs, in reality it forms a distinct barrier of nonnegligible width for both electrons and holes. This is indicated schematically in Fig. 8. Although current flow at low biases will largely be the result of the thermionic emission of electrons and holes over the relevant InAlAs barrier, conduction by field assisted tunneling will increasingly occur at higher biases. The details of the InAlAs tunnel barriers will profoundly influence the form of the I-V curve. If present, an intermediate compositionally graded or "chirped" superlattice layer will also affect the I-V characteristic.

Although a two-dimensional analysis incorporating the details of the barriers is necessary for a full understanding of the I-V characteristic, it is nevertheless interesting to examine the extent to which a simple one-dimensional analysis [27] models the experimental situation. We expect the "effective" electron barrier at the contacts to approach the value of the Schottky height on InAlAs; to be slightly lower to account for some tunneling through the barrier and some image charge lowering [29], but nevertheless to be greater than the difference between the InAlAs Schottky height and the InGaAs-InAlAs conduction band offset (~0.51 V [30]). If we take a value of 0.82 V for the Schottky barrier height, as measured for Au-InGaAs [23], this places the effective electron barrier between 0.31 and 0.82 V. Similarly, the effective hole barrier at the electrode will be greater than ~0.42 V (E_g {InAlAs} − φ_{Bn}{InAlAs-metal}−ΔE_v{InGaAs-InAlAs}), and approach 0.66 V (E_g{InAlAs}−φ_{Bn}{InAlAs-metal}).

If we use the simplest thermionic emission analysis, and ignore the details of the InAlAs barriers and all tunneling contributions, we obtain an expression for the current [27]:

$$J = A_n^* T^2 \exp(-e\{\varphi_n - \Delta\varphi_n\}/kT) + A_p^* T^2 \exp(-e\{\varphi_p - \Delta\varphi_p\}/kT) \quad (3)$$

where, $A_{n,p}^*$ are the effective Richardson constants for the electrons and holes, respectively, $\varphi_{n,p}$ are the respective barrier heights, and $\Delta\varphi_{n,p}$ are the barrier lowerings caused by image charge effects—for a simple Schottky contact, $\Delta\varphi_{n,p} = \sqrt{(eV/4\pi\epsilon L)}$. The carrier species injected over the lower barrier will dominate the current flow. If we assume (*a posteriori*) that hole conduction predominates, and take a value of 49 $A/cm^2/K^2$ for A_p^* in InGaAs, the zero bias extrapolated current of the I-V curve in Fig. 7 yields an effective hole barrier of ~0.63 V. I-V curves of other devices with ~300–800 Å (as-grown) InAlAs layers yield similar values. Allowing for a reduction of A_p^* due to carrier back-reflection [29], a corrected value in the region of ~0.6 V is suggested. This justifies the above assertion that the hole current dominates.

A preliminary examination of the temperature dependence of the low bias portion of the dark current curve suggests the effective barrier height is in the region of 0.5–0.7 V [31], though the nature of the I-V curves makes this determination somewhat imprecise. An examination of the forward current of an enhanced barrier detector which used a 600 Å thick chirped InAlAs-InGaAs superlattice [21] and a Au electrode in a single Schottky diode yielded an effective electron barrier of ~0.7 V with an ideality factor of 1.19 (using an A_n^* value of 7.03 $A/cm^2/K^2$). A lower effective Richardson constant, to allow for carrier reflection, would reduce this value somewhat; however the value of 0.7 V was also in agreement with C-V measurements. This figure compliments the value of 0.6–0.65 V suggested above for the effective hole barrier. We thus see that, as expected, the effect of the InAlAs is to raise both the electron and hole barriers to values close to those of the Schottky barrier heights on the InAlAs. The barrier potentials obtained also suggest that the holes dominate the carrier transport in the MSM.

The simple Schottky barrier model provides an understanding of the low bias portion of the I-V characteristic. However, tunneling through the InAlAs barrier is required to explain the rapid rise of the dark current with increasing bias, as seen in Fig. 7, and also the "soft" breakdown characteristic. The tunnel current component of the leakage current rises steeply as the voltage dropped across the enhancement barrier reduces the effective barrier height(s) and then, with increasing bias, yields

Authorized licensed use limited to: IEEE Xplore. Downloaded on March 4, 2009 at 03:08 from IEEE Xplore. Restrictions apply.

triangular barriers of diminishing width; the exponential dependence of the tunnel current on the barrier height and width results in a rapidly rising I–V curve. Again, hole conduction will dominate. A significant surface current component can be largely ruled out because no change was observed in similar devices when the semiconductor between the fingers was etched down into the InGaAs. A tunnelling current calculation using the potential dropped across the barrier layer in the two-dimensional structure predicts a slope for the Log(I) versus V curve similar to that seen in the figure [32].

Soft breakdown of the 2 μm spacing device in Fig. 7 starts to occur at $\sim$30–40 V, and in a very repeatable fashion. Although there was no recess etching between the fingers in this device, as mentioned above, where this *was* done no change was been observed in the characteristic. Breakdown would therefore appear to arise from current flow across the barrier. Avalanche has often been cited as a potential source of breakdown [16], [22], [28]; the spacings between the fingers have sometimes been recessed [28] and rounded electrode structures have even been used [15]. However, the breakdown biases observed experimentally are rather lower than those expected for avalanching, but are consistent with the dominance of a tunnel current through trapezoidal InAlAs barriers. The "soft" nature of the breakdown, together with the fact that the bias required for breakdown decreases and the current above breakdown increases as the temperature is raised [32], also argue that a tunneling mechanism is primarily responsible. (A negative temperature coefficient would be expected if avalanching were occurring.)

We do note, however, that the fields required for avalanching are being approached at the highest biases used. The bias to initiate avalanching is rather lower than suggested by a one-dimensional calculation (which is 60–100 V for an InGaAs "slab" of 2 μm thickness, equal to the interdigital spacing) because the electric field strength is much higher near the edges of the contacts. The presence of the wider gap InAlAs under the electrodes may have some effect in limiting the onset of the breakdown. When breakdown does occur, be it tunneling or avalanche, it will be concentrated near the periphery of the electrodes, most probably at the finger tips where the field is likely to be strongest. The high biases indicated for "breakdown" in the experimental device shown in Fig. 7 is, of course, testament to the high quality of the OMCVD grown layer of that device.

A complete understanding and prediction of the dark current curve of the planar MSM requires an accurate description of the potential barriers which exist under the electrodes, and must incorporate both thermionic and tunneling current components. A fully two-dimensional analysis of the electric field and conduction current density is also required.

For the receiver engineer, an important point is that the dark current at operating biases in the InAlAs–InGaAs MSM is now so low that the associated shot noise may be effectively ignored in receiver design. For biases of up to $\sim$20 V, less than 0.06 pA/$\sqrt{\text{Hz}}$ will be generated in the detector graphed in Fig. 7 (active area, 25 × 25 μm), which is between one and two orders of magnitude lower than the equivalent input noise of state-of-the-art receivers. The introduction of the InAlAs layer has thus produced an InGaAs MSM detector which is suitable for use in a state-of-the-art low noise receiver.

IV. Photoresponse

The CW photoresponse of a typical InAlAs–InGaAs MSM is shown in Fig. 9 for light of different incident powers. The shoulder at 1–1.5 V occurs because, as discussed in the previous section, sufficient bias must be applied to obtain flat band at the anode and separate the generated carriers. After the knee, a fairly flat photoresponse is found, rising gently as the bias is increased. At the lower biases this is largely due to the increase of the depletion volume—the C–V curve is similar to that shown in Fig. 6. At $\sim$7 V the internal quantum efficiency, as calculated from the fractional surface area exposed and the known penetration depth of the light [33], assumes a value of unity. At higher biases the photoresponse continues to rise slowly. We therefore have some net internal gain present at these higher biases. Some gain is also presumably present at lower biases but is masked by the incomplete depletion of the absorption region.

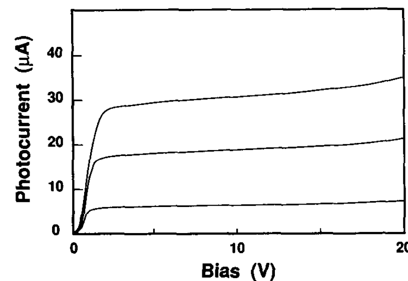

Fig. 9. Photoresponse of a "1 × 2" InAlAs–InGaAs MSM for different incident light intensities. The dark current is coincident with the x axis.

Gain has been observed in both GaAs [8], [28], [34] and barrier-enhanced InGaAs MSM's [11], [12], [15]–[17], [20], [22]. In the former, it has been attributed to traps in the GaAs and at the substrate, electrode, and air interfaces [7], [8], [28], [34]. It has also been speculated that a modulation of the conduction band edge under the anode might be responsible [8], however an investigation of the field in this region shows that this is unlikely. Trap densities within the absorption material can be minimized by using high quality detector material and, perhaps, a suitable substrate buffer layer; an AlGaAs substrate buffer layer used in conjunction with an AlGaAs capping surface layer to reduce surface traps has been shown to reduce the gain in GaAs MSM's [7].

In an early report of ours [11] of an InGaAs MSM using a strained GaAs layer for barrier enhancement, significant gain was observed (up to $\sim$300%) and attributed to traps at the GaAs–InGaAs heterointerface and within the GaAs layer. With the use of high quality lattice-matched InAlAs with a low interfacial trap density, this internal gain is reduced to a very low level. For the device in Fig. 9, the photocurrent rises by less than 10% of its unity gain value for biases up to $\sim$20 V, and by only $\sim$40% at the onset of breakdown. In Section VI we show that the noise in the lattice-matched InAlAs–InGaAs device under normal operating conditions is sufficiently low not to introduce a sensitivity penalty to a receiver operating at typical frequencies.

Carrier trapping due to an unintentional interfacial oxide barrier under the electrodes has in the past been blamed for the presence of gain in MSM devices, as this can cause carrier injection from the electrodes. The InAlAs heterobarrier layer provides a structure where both electrons and holes may become confined by the band potentials. Presuming a low trap density and no unintentional oxide formation during (or after) fabrication, charge trapped at the heterointerface may be one of the carrier contributors to the remaining internal gain. We also note that carrier pileup will slow down the detector response. Pileup

Authorized licensed use limited to: IEEE Xplore. Downloaded on March 4, 2009 at 03:08 from IEEE Xplore. Restrictions apply.

may be completely avoided by grading out the band offsets at the InAlAs–InGaAs heterointerface [35].

The photoresponse was found to increase linearly with the light intensity, up to a power of ~1.5 mW (the highest level used) [32] when the device was illuminated evenly over the ~25 × 25 μm interdigitated area. Power saturation effects might be expected to occur at higher power levels due to space charge buildup within the detector. The MSM might be expected to be more sensitive than the planar p–i–n to high power levels because of the fringing nature of the electric field. The response of the MSM at high optical powers has not been studied in detail to date, and this needs to be done before the detector can be used in certain applications, for example in coherent systems with local oscillator powers of >> 1 mW.

V. Quantum Efficiency

The internal quantum efficiency of the MSM is close to unity over most of the operating range, as discussed in the last section, with some small gain present at the higher biases. The external quantum efficiency is therefore simply determined by the electrode structure (the electrodes are generally made thick enough to be opaque) and the thickness of the InGaAs. The external quantum efficiency is given by

$$\eta = (1 - r) \frac{s}{s + w} (1 - \exp[-d/\mathcal{L}]) \quad (4)$$

where w is the finger width, s is the interdigital spacing, $\mathcal{L}$ is the optical penetration length at the wavelength used, and d is the InGaAs thickness. The Fresnel reflectivity r is included but may be reduced to zero with the use of an antireflection coating. Fig. 10 plots the external efficiency calculated for "1 × 1," "1 × 2," and "1 × 3" AR-coated detectors as a function of InGaAs thickness, for both 1.3 and 1.55 μm wavelength incident light. The "limiting" efficiency, corresponding to a detector with infinitely narrow electrodes (or any device under back illumination), is also shown.

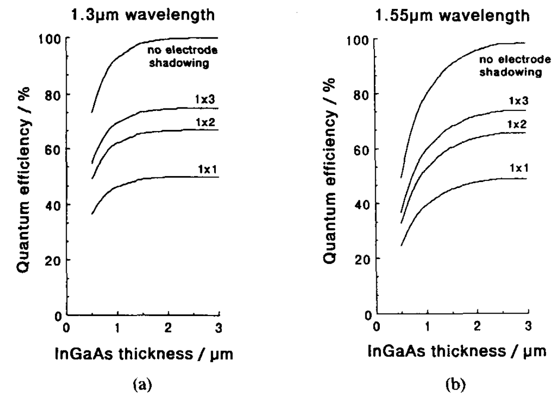

Fig. 10. External quantum efficiency of the AR-coated MSM as a function of InGaAs thickness at 1.3 μm and 1.55 μm wavelength. For "1 × 1," "1 × 2," and "1 × 3" electrode structures. The limiting cases of zero width electrodes are also plotted.

The shadowing of the active area by the electrodes and the consequent loss of efficiency is a main drawback of the MSM structure. Electron beam writing techniques may be employed to produce sub-μm width fingers which will minimize the loss, and the writing stage could be combined with FET gate definition in the fabrication of an integrated amplifier, however routine photolithographic processes limit the finger widths to close to a 1 μm. Semitransparent electrodes may be used to increase the quantum efficiency, though this is generally undesirable as it leads to a slower response as carriers generated under the electrodes suffer longer transit times (see Section III); they may be employed, however, where high speed is not of prime importance. The same applies to back illumination through the transparent InP substrate, which of course eliminates electrode reflection loss entirely.

It might be mentioned here that there are a number of ways in which the quantum efficiency of the MSM with a given electrode structure, and indeed that of a conventional p–i–n, might be increased without a loss of bandwidth. The simplest, perhaps, is to pass the incident light twice through the device by using a back reflector. For the MSM detector in particular, a semiconductor reflector stack grown directly under the absorption layer is desirable, rather than a reflector on the back-side of the wafer, as the reflected light must remain for the most part illuminating the absorption region between the fingers and not under them. This double-pass structure may be extended to a multiple pass one with the introduction of a top surface reflector and the consequent formation of a low Q cavity. This requires just a very thin absorption region to obtain a very high quantum efficiency. A waveguide detector geometry [36], to be discussed in Section VIII, also offers the potential of near unity quantum efficiency, though because carriers are generated under the electrode fingers there is inevitably some sacrifice of bandwidth, the temporal response being similar to that obtained in the back-illuminated detector. A similar compromise occurs if one uses a surface grating to diffract incident light into the InGaAs at a high angle to the normal in order to reduce the surface-normal penetration depth.

A more speculative way to increase the quantum efficiency is the use of lattice mismatched $In_xGa_{1-x}As$, where $x > 0.53$. This might be expected to absorb the light more strongly than $In_{0.53}Ga_{0.47}As$ lattice matched to InP, though some degradation of the dc characteristic and the response speed from traps associated with the strained absorption layer is a distinct possibility. Another method might be the excitation of a bound electromagnetic resonance in the vicinity of the top surface, for example a surface or local plasmon mode or a localized guided mode [37], [38]. This would have the effect of localizing the detector absorption in the uppermost portion of the InGaAs and would lead to an enhanced efficiency in a thin detector [39]. MSM's with gold spheres touching the surface have been demonstrated to increase the quantum efficiency [40], [41], though in these particular cases local plasmon modes were not primarily responsible.

VI. Device Noise

The noise generated in the photodetector front-end of a receiver can have a significant impact on the overall system performance. Commonly, the noise components are assumed to have a white spectral power density; for example the shot noise of a p–n junction or the thermal noise generated by a base resistance or the channel of a field effect transistor [6], [42].

For p–i–n detectors, the thermal noise component generated by the series resistance can be neglected and the noise behavior is dominated by the shot noise of the dark leakage current and the light-dependent shot noise induced by the arriving signal. To first order, the same applies to the planar MSM detectors.

Authorized licensed use limited to: IEEE Xplore. Downloaded on March 4, 2009 at 03:08 from IEEE Xplore. Restrictions apply.

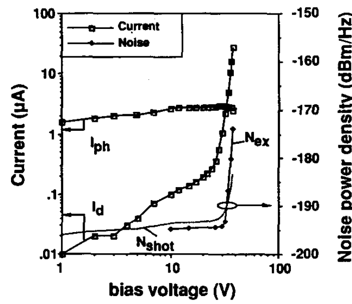

Fig. 11. The noise power N_{ex} measured at 10 MHz for an InAlAs-InGaAs MSM under illumination. The shot noise associated with the detector current (photocurrent + dark current) is plotted, as N_{shot}. The dark current I_d and photocurrent I_{ph} are also shown. The detector uses a 500 Å lattice matched InAlAs layer and has 3 μm finger spacings.

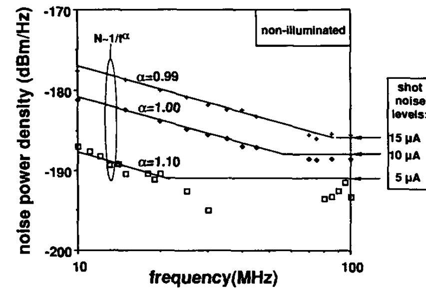

Fig. 12. Spectral dependence of the noise of the nonilluminated detector in Fig. 11 for the three operating points in the soft-breakdown region indicated by the solid squares in that figure. Total detector currents are 5, 10, and 15 μA.

However, while a conventional pin photodiode has a "vertical" current flow, the MSM detector has a lateral current flow with strong interactions with the surface and the semiconductor interfaces, much like a FET. In FET's, a low-frequency component with a $1/f^{\alpha}$-like dependence, where α is an empirical parameter often close to unity, is the dominating noise source at low frequencies, its cut-off frequency being dependent on the FET fabrication and geometry [43], [44]. A similar low-frequency noise behavior is therefore expected in MSM's, in particular the barrier enhanced device.

An excess noise at 30 MHz has been observed in GaAs MSM detectors [45], accompanying the onset and subsequent increase of internal gain. The spectral dependence of this noise component, however, was not investigated. An InGaAs MSM which employed a strained GaAs enhancement layer [46] was shown to have significantly more noise than the shot noise component at frequencies below 35 MHz, and these devices also showed significant low-frequency gain. It thus appears likely that excess noise, as well as most of the internal gain, is caused by traps. In the case of the InGaAs MSM in [46], these presumably occurred predominantly at the GaAs-InGaAs interface and within the GaAs layer itself.

The noise characteristics of an OMCVD grown InAlAs-InGaAs lattice-matched MSM are shown in Figs. 11-14. The low frequency noise performance is far superior to that of the strained GaAs barrier device in [46]. There is also very little low frequency gain.

Fig. 11 shows the noise power density at 10 MHz for a typical detector under illumination. It is given as a spectral power density into a 50 Ω load, and is labeled N_{ex}. This device had a 500 Å InAlAs layer and 3 μm electrode spacings. The dark current I_d and photocurrent I_{ph} are also shown, and the shot noise associated with the total current, $I_{ph} + I_d$, is plotted as N_{shot}. We see that the measured noise follows the calculated shot noise for biases up to 30 V (the small offset is due to noncompensated loss in the microwave probe head and cable to the bias network), but that as the detector approaches soft breakdown at $V > 30$ V, excess noise above this shot noise limit is introduced. Experimentally, N_{ex} was found to increase as $(I_{ph} + I_d)^{2.4}$ in this region, rather than $(I_{ph} + I_d)^1$, as expected from shot noise behavior. We also note that at $> \sim 10$ V bias the calculated internal efficiency was ~100% and that there is no significant slope to the photocurrent curve at high biases, indicating that there is no significant internal gain occuring over the 10-30 V bias range.

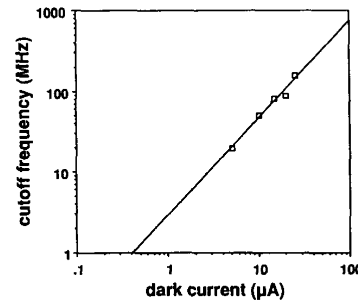

Fig. 13. Plot of the cut-off frequency for low frequency excess noise F_c, against detector dark current.

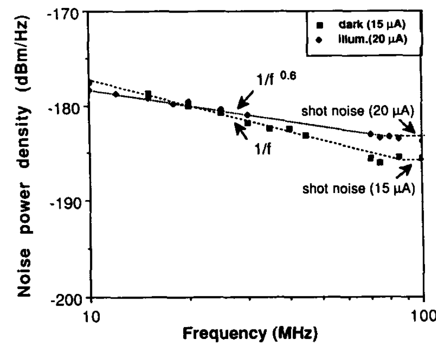

Fig. 14. Comparison the spectral characteristics of the noise for the illuminated and nonilluminated device. Light sufficient to generate a 5 μA photocurrent is incident on the detector which is biased to give a dark current of 15 μA.

Fig. 11 shows that there is *some* excess noise at 10 MHz at applied biases close to breakdown. Fig. 12 plots the spectral dependence, from 10 to 100 MHz, of the noise for three operating points in this soft breakdown region (the points indicated by the solid squares in Fig. 11). The detector is not illuminated. We see that at high frequencies the noise is shot-like, the theoretical shot-noise power density being indicated by the horizontal portion of the lines drawn on the graph. At lower frequencies, an excess noise component is present. This appears to vary as $1/f^{\alpha}$, with a value of α close to 1. The "corner frequency" f_c below which the $1/f$ excess noise becomes sig-

Authorized licensed use limited to: IEEE Xplore. Downloaded on March 4, 2009 at 03:08 from IEEE Xplore. Restrictions apply.

nificant, is plotted in Fig. 13 as a function of the detector current. The curve is extrapolated to lower detector currents, approaching typical operating conditions. For this detector, the dark current at a normal operating bias (i.e., that bias sufficient to obtain effective depletion and a fast detector response; see next section) would be in the region of 100 nA; Fig. 13 indicates that for this current only shot noise will be present down to frequencies below 1 MHz.

It should be noted that the $1/f$ cut-off frequency is not a function of the detector current but rather of the bias [45]. It most probably depends, in fact, on the strength and distribution of the electric field within the InGaAs, with greatest importance attached to the presence of regions with higher field strengths. As these latter occur near the surface and are largely determined by the value of the applied bias divided by the interdigital spacing (with the electrode width playing a minor perturbatory role), this "normalized" bias figure is expected to determine the character of the noise present in the detector and to be 'universal' in application to devices with different dimensions. The degree of the internal gain present and the dark current density will also be functions of this "normalized" bias. As Figs. 11–13 show that only shot noise is present above ~1 MHz at the unity gain point—the usual operating point for the detector—for the device under study, it is thus likely that no excess noise will be present below ~1 MHz in *any* device when operated under these standard conditions.

Fig. 14 compares the noise spectrum of the nonilluminated device with that of the illuminated detector. In order to study the excess noise component, a bias point in the soft-breakdown region was taken—the bias for 15 μA of dark current (as in Fig. 12)—and the detector then illuminated to give a photocurrent of 5 μA. We find that when light is present the excess noise component is somewhat suppressed. This is probably because the photogenerated carriers satisfy a fraction of the traps associated with the excess noise. Within the accuracy of the measurement, the cut-off frequency remains fixed and the high frequency noise merely increases in accord with the increased shot noise of the detector current.

We may thus conclude that InGaAs MSM detectors using a high-quality lattice-matched InAlAs barrier enhancement layer show a shot-noise dominated behavior at frequencies as low as ~1 MHz under normal operating conditions. The excess $1/f^{\alpha}$ noise component which is observed at low frequencies and high biases close to breakdown may be neglected for the vast majority of analogue and broad-band digital optical communications system applications.

VII. Temporal Response

As discussed in Section II, one of the advantages of the planar MSM structure is its low capacitance per unit area. From Fig. 3, we see that a detector designed for simple fiber coupling, with an edge length of several tens of μm, will have a capacitance of much less than 100 fF. This corresponds to an RC charging time into 50 Ω of less than 5 ps. The transit times of the photo-generated carriers, on the other hand, are on the order of [(electrode separation)/(2 × saturation carrier velocity)], which for devices with 1–3 μm finger separations is 8–24 ps, assuming an average saturation velocities of ~6 × 10^4 m/s (taken from [47]). Thus, for typical photolithographically defined devices with active areas of a few tens of μm on a side, the transit times of the generated carriers will limit the speed of response. Only with a high impedance receiver front end might the RC charging time be significant in determining the bandwidth. Most of the MSM detectors reported to date have had their electrode pattern defined by standard photolithographic procedures and have been of a size suitable for coupling to a single-mode fiber; they have all been transit-time limited. It should be noted, however, that if the detector is either much larger, or employs highly submicron finger spacings, the capacitance may become large enough to limit the speed. In the analysis presented below, we assume that this is not the case, and we examine the speed limitations imposed by the transit times of the photogenerated carriers.

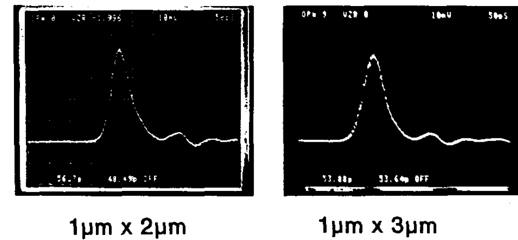

Fig. 15. Pulse response, under identical experimental conditions, of a "1 × 2" and a "1 × 3" detector fabricated next to each other on the same chip. Front-illuminating 1.3 μm light with 15 V detector bias. The system response width is ~40 ps.

The carrier transit-time limitation is clearly demonstrated in Fig. 15. This compares the response of two detectors under identical conditions; one with 2 μm electrode spacings and one with 3 μm spacings, both fabricated side-by-side on the same chip. The 3 μm spacing device is slower, giving a 54 ps pulsewidth (FWHM) against 49 ps for the 2 μm device. This small fractional increase actually represents a significant decrease in the detector speed because the majority of the pulsewidth (some 40 ps) is the finite system width—the exciting optical pulse width and the measurement system response width.

In order to investigate the speed limitation imposed by the finite carrier transit times, the carrier motion must be modeled. The transit-time limited response of the surface illuminated p–i–n has been examined in some detail [47], [48]. Using the formulations developed for the p–i–n [(1) in [47] and [48]] we can obtain an upper bound to the transit-time limited bandwidth of the MSM; this is equal to the bandwidth of the p–i–n for which the optical penetration depth is much greater than the thickness of the intrinsic region (in this p–i–n response model, the absorption is restricted to the intrinsic region, which is assumed depleted). The corresponding MSM is the one where the interdigital spacing is equal to the thickness of the p–i–n intrinsic region. In Fig. 16(a) we plot the (3 dB, electrical power) bandwidth obtained as a function of this "electrode spacing;" an electron velocity of 7 × 10^6 cm/s and a hole velocity of 5 × 10^6 cm/s was used. In Fig. 16(b) we graph the 3 dB $R_{50\Omega}C$-limited bandwidth of the MSM's shown in Fig. 3 as a function of the side length of the interdigitated area. A comparison of Fig. 16(a) and (b) confirms that the speed of a typical sized MSM into a moderate load impedance is limited by carrier transit times.

The above transit-time analysis is for a "one-dimensional" detector. Other "one-dimensional MSM" calculations have been reported for GaAs devices, using both Monte Carlo and quantum mechanical approaches [49], as well as calculations which incorporate diffusion and recombination effects [28]. However, the thickness of the InGaAs in an MSM used in op-

Authorized licensed use limited to: IEEE Xplore. Downloaded on March 4, 2009 at 03:08 from IEEE Xplore. Restrictions apply.

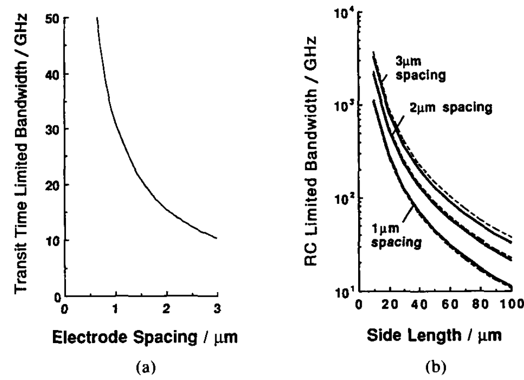

Fig. 16. (a) Transit-time limited bandwidth of a one-dimensional detector, obtained by assuming uniform carrier generation between the electrodes, and electron and hole drift velocities of, respectively, 7×10^6 cm/s and 5×10^6 cm/s. (b) *RC* limited bandwidth of MSM's with 1, 2, and 3 μm interdigital spacings into 50 Ω, plotted as a function of the side length of the interdigitated region. The solid line assumes a 1 μm electrode width and the dashed lines take a 0.5 μm width. The plots correspond to the device capacitances graphed in Fig. 3.

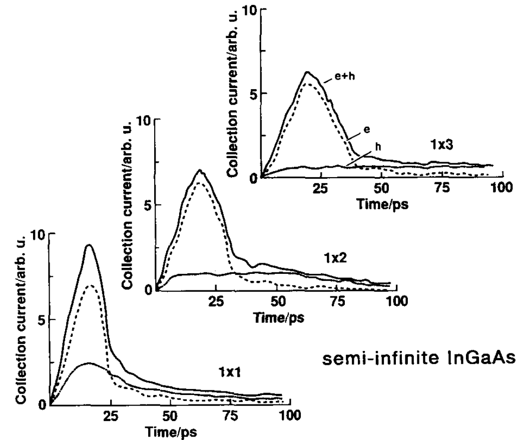

Fig. 17. Computed collection currents of "1 × 1," "1 × 2," and "1 × 3" InGaAs MSM's; for 1.55 μm front illumination, 10 V bias, and "semiinfinite" InGaAs. The separate electron and hole currents are also shown, dashed and dotted-dashed lines, respectively.

tical communications must generally be ≥ 1 μm so that the layer absorbs a large fraction of the incident light and yields a high quantum efficiency (penetration lengths, 0.87 μm at 1.3 μm and 1.47 μm at 1.55 μm). In this case, a one-dimensional calculation is not sufficient for the typical MSM with a 1–3 μm finger spacing, and a two-dimensional calculation is required.

The finite thickness of the InGaAs layer leads to curved carrier paths which are longer than in the one-dimensional approximation. This results in longer transit times and a slower response. The speed of the detector is determined by the detector geometry and the applied bias. It is also a function of the incident wavelength as this determines the vertical distribution of the carrier generation. The wavelength dependence of the response has often been overlooked in examinations of the pulse response of the MSM. This dependence means that the pulse response and bandwidth determined at one wavelength will not generally be the same as that which occurs at another. The form of the enhancement barrier and the incident optical power level may also influence the speed of the detector.

A model based on the two-dimensional drift of photogenerated carriers [50] gives a good description of the response for a typical InGaAs MSM under usual operating conditions. Carrier diffusion may be ignored at normal operating biases. The high crystal quality of the InAlAs–InGaAs detector also allows us to neglect recombination and charge trapping. The steady drift of carriers along the field lines is expected to be a fairly good approximation to the actual carrier motion for devices with electrode spacings and an absorption layer thickness of ≥ 1 μm. Ballistic effects and carrier scattering are expected to provide only a modest modification to this motion. Velocity overshoot may be ignored in devices with supra-μm dimensions [51]. Quantum mechanical effects are also presumed to be of minor significance. Additional speed limitations arising from electrical LCR parasitics may be added empirically using an appropriate equivalent circuit model.

Figs. 17–19 give the calculated transit-time limited response of typical InGaAs MSM detectors front-illuminated with 1.55 μm wavelength light. The two-dimensional carrier drift is computed using the steady state field-dependent carrier velocities

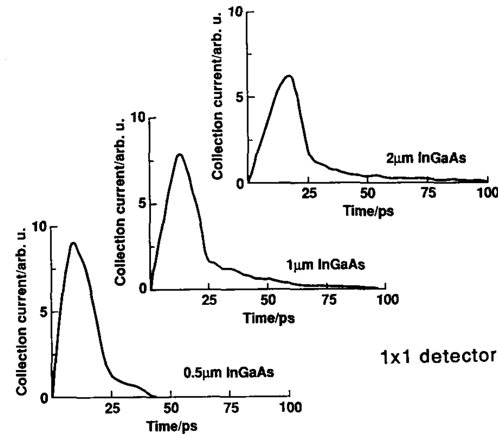

Fig. 18. Collection current in a "1 × 1" InGaAs MSM with different absorption layer thicknesses. Again, for 1.55 μm light and 10 V bias.

compiled in [47] and an initial photocarrier concentration determined by the optical penetration length. The applied bias is 10 V and the InGaAs is assumed to be undoped.

Fig. 17 shows how the "collection current" at the electrodes evolve with time after an optical impulse strikes the detector at $t = 0$. The response of MSM's with "semiinfinite" InGaAs (i.e., thicker than a few optical penetration lengths) and 1, 2, and 3 μm electrode spacings are given. The separate electron and hole currents are also shown. What is most striking from these plots is the difference between the electron and hole collection currents. The electrons are collected quite quickly, by-and-large within the first 40 ps, while the holes are collected much more slowly; a peaked hole response occurs only for the 1 μm spacing detector and the peak rapidly broadens as the electrode spacing increases so that the response is virtually flat out to beyond $t = 100$ ps in the 3 μm spacing detector. The reason for this is that the holes have a much lower velocity when the electric field strength is low, at $E < 5$ V/μm (Fig. 1 in [47]).

Authorized licensed use limited to: IEEE Xplore. Downloaded on March 4, 2009 at 03:08 from IEEE Xplore. Restrictions apply.

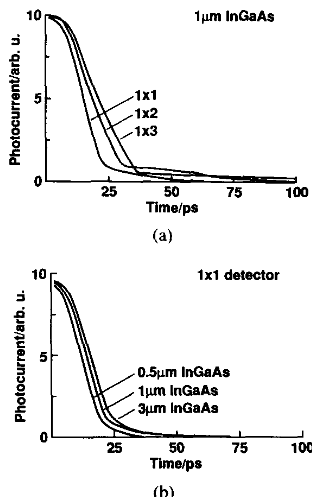

Fig. 19. (a) Impulse response of "1 × 1," "1 × 2," and "1 × 3" detectors with 1 μm thick InGaAs. For 1.55 μm light and 10 V bias. (b) Impulse response of the "1 × 1" device with different InGaAs layer thicknesses. Again, for 1.55 μm light and 10 V bias.

For the detector geometries and the applied bias in this example, the photogenerated holes penetrate regions of low electric field where they travel much more slowly. In contrast, the electrons in the same regions generally travel close to, or at, their saturation velocity. The lower saturation velocity of the holes in the high field regions also conspires to slow down the hole collection, though in comparison to the above this has only a minor effect.

Practical detectors do not consist of a semiinfinite absorption layer, but rather a thin epilayer of InGaAs, typically 0.5–2 μm, grown on an InP substrate. The finite thickness of the InGaAs modifies the carrier paths. A fraction of the higher energy electrons will surmount the barrier provided by the conduction band offset and travel within the InP, although the electrostatic attraction to the holes in the InGaAs will tend to limit their excursion from the interface. However, the holes and the lower energy electrons will be more-or-less confined to the InGaAs by the band offset at the InGaAs–InP heterointerface. The important consequence of this is that the holes which would have penetrated deep into the InGaAs in a thicker device are now restricted to travel along the InGaAs–InP interface before returning into the bulk InGaAs on passage to the negatively biased electrode. This has the practical effect of eliminating the longest of the carrier transit times. Fig. 18 shows a calculation of the collection current in detectors with a finite thickness of InGaAs. Carrier motion is approximated by assuming that neither the electrons nor holes can pass into the InP. As expected, we observe that the tail of the "response" is reduced as the InGaAs thickness decreases.

Although the "collection current" tells us much about the carrier dynamics within the MSM, it is not a direct measure of the photoresponse. This is given by the integrated displacement current density at the electrode contacts. We may calculate this from the motion of the photocarriers by using a conformal mapping technique to transform the carrier motion in the interdigitated detector to that in a parallel plate geometry [26]; in this latter the displacement current may be evaluated easily [52]. Impulse responses calculated from the transformed carrier motions are given in Fig. 19. Fig. 19(a) shows how the response of the 1 μm InGaAs device varies with electrode spacing and Fig. 19(b) shows the dependence of the response of the "1 × 1" detector on the InGaAs thickness. The expected trends are observed. Increasing the electrode separation broadens the pulse response (the tails are again the result of the slow moving holes). Increasing the absorption layer thickness also broadens the response slightly, though the effect is minimal at > ~2 μm thickness, which might be expected from a consideration of the field profile and the initial carrier distribution; it is also less for devices with a larger interelectrode spacing because the fractional change of the carrier motion is correspondingly smaller.

As mentioned above, the response is expected to be a function of the incident wavelength because this determines the distribution of the initial carrier concentration. The extent of the wavelength dependence depends on how significantly the changing distribution of generated carriers affects the overall carrier paths, which is a function of the InGaAs thickness, the electrode spacing, and, to some extent, also of the electrode widths. Although the penetration of 1.3 and 1.55 μm light differs by almost a factor of 2, the difference in the computed impulse response in typical detectors is fairly modest. For example, the computed pulsewidth of a "1 × 1" detector with 2 μm of InGaAs is just ~3 ps narrower for 1.3 μm light than for 1.55 μm light, and this difference decreases as the electrode spacing gets larger. For much shorter wavelengths, however, the optical penetration into the InGaAs is much shallower and the detector assumes a quasi-one-dimensional operation with a significantly faster response. For very thin InGaAs devices, the wavelength dependence also vanishes as carriers are generated more or less evenly across the absorption layer. We should note, however, that surface effects such as carrier trapping and recombination with possibly attendant current gain and noise, will tend to play an increased role.

An experimental pulse response is given in Fig. 20 (solid line). The device is a "1 × 2" InAlAs(500 Å)–InGaAs (1.3 μm) detector grown by low pressure OMCVD. No InAlAs–InGaAs interface grading was employed. The calculated response is also shown (dashed line), being a convolution of the computed impulse response and the measured system response (~40 ps response width). The calculated impulse responses are in fairly good agreement with measured detector pulsewidths. Although a close comparison between experiment and theory is unfortunately not possible because the system width is a significant fraction of the measured experimental pulsewidth, it does appear that the two-dimensional drift model used in the calculation gives a reasonably accurate prediction of the MSM response. The variation of the response with the interdigital spacing and InGaAs layer thickness given in Fig. 19 may therefore be taken as a reasonably accurate design guide for actual detector performance.

The width and general form of the experimental response in Fig. 20 is in agreement with calculation. However, we do notice that the trailing edge of the experimental response, at around t_{peak} + 50 ps, is somewhat raised in comparison with the theory. (The oscillations later are due to resonances associated with the measurement setup, and should be ignored). This is probably a consequence of carrier pile up at the InAlAs–InGaAs heterointerface. Carrier pile up is a recognized problem in avalanche photodiodes [35], where holes confined by the heterointerface lead to a reduction in the bandwidth, and more recently in heterostructure modulators [53], [54], where it also leads to a re-

Authorized licensed use limited to: IEEE Xplore. Downloaded on March 4, 2009 at 03:08 from IEEE Xplore. Restrictions apply.

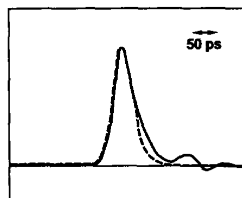

Fig. 20. Comparison between an experimental pulse response (solid line) and a two-dimensional transit-time carrier drift model. The detector is a "1 × 2" device with 1.3 μm of InGaAs and under 1.3 μm wavelength front illumination.

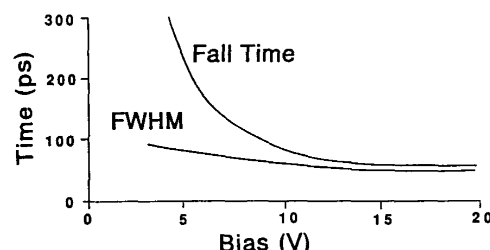

Fig. 21. Variation of the pulsewidth (FWHM) and fall time (90–10%) of a "1 × 2," 1.3 μm InGaAs, detector as a function of applied bias. InGaAs doping level, n $\sim 8 \times 10^{14}$ cm^{-3}.

duction in the modulation contrast. In the InAlAs–InGaAs MSM, the electrons may present the more serious problem, as they encounter a higher barrier potential, though hole "pile up" may be significant at higher biases when the larger hole effective mass decreases their relative tunneling rate. Some evidence for carrier pile up is provided by the fact that a reduction in the trailing edge is observed when the device is heated [32]. We also note that the highest bandwidths reported to date [55] have been for a detector which incorporates a rather "leaky" strained layer of GaAs as the barrier enhancement layer.

It should be possible to eliminate charge trapping completely by grading out the InAlAs–InGaAs band offset using compositionally graded InGaAlAs without sacrificing the low dark current. There has been a report of a graded barrier device [22], though in this case a slow pulse response with a long tail portion was observed, presumably the result of somewhat poorer crystal quality; the leakage current in this case was also rather high. There has also been one report of an InAlAs–InGaAs device which uses a chirped InAlAs–InGaAs superlattice for barrier enhancement [17], but in this case the response also showed a long flat tail, extending to beyond 100 ps. This is possibly caused by the slow sweep out of carriers across the barriers, or may be the result of carrier trapping at the many interfaces present.

We note that a significant bias must be applied to the MSM detector in order to obtain a fast response. As discussed above, this is because the applied field must both effectively deplete the InGaAs and then impose a field sufficient to provide high carrier drift velocities. Only when a bias sufficient for "complete" high velocity transport is applied can the full speed of the device be realized. Fig. 21 shows how the pulsewidth (FWHM) and fall time (90–10%) of a "1 × 2" detector decreases as the applied bias is increased. The C–V plot for this device was similar to that shown in Fig. 6.

The fact that the full speed potential of the MSM may not be realized until a significant bias is applied must be borne in mind when designing the device for high speed operation, and in particular when considering its integration into a monolithic receiver circuit with a single supply rail. A smaller interdigital spacing in conjunction with a thin InGaAs layer (and a lower background doping level) will reduce the bias required for high speed operation.

The sensitivity of detector speed to regions of weak lateral electric field makes the bandwidth of the MSM more sensitive to high incident optical power levels than a comparable and similarly biased p–i–n. However, this may be offset by the fact that the illuminated area of the MSM can be much larger. A 10 mW signal, delivered via a cleaved fiber to a typical device, will introduce local carrier concentrations in the region of only the mid 10^{16} cm^{-3}, and this space charge level would not be expected to adversely affect photo-carrier transport. Experimentally, we have detected no perceptible decrease in the pulse response width for incident power levels up to 1–2 mW, the highest powers we have investigated [32].

For many applications, in particular analogue systems, the bandwidth of the photodetector is a crucial parameter. For a p–i–n diode analytic expressions are readily available and the bandwidth may be calculated directly. For the MSM detector, however, the frequency response must be obtained by numerically transforming the computed impulse response,

$$P(\omega) = |\mathfrak{F}\{f(t)\}|^2. \quad (5)$$

The 3 dB point (photocurrent down by $\sqrt{2}$) calculated for the "1 × 1," "1 × 2," and "1 × 3" detector responses shown in Fig. 19(a) are given in Fig. 22(a). The estimated uncertainty is ± 1 GHz. The bandwidths of the "1 × 1" detector pulses shown as a function of InGaAs thickness in Fig. 19(b), are given in Fig. 22(b).

Of particular interest in the design of a photoreceiver is the trade off which occurs between speed and efficiency. This has been extensively examined for the p–i–n diode [47], where the intrinsic layer thickness determines both the quantum efficiency and the maximum (transit-time limited) bandwidth; to obtain this maximum speed the detector area must simply be made small enough to ensure capacitive effects are negligible—fabrication and light-coupling permitting. For the MSM detector, we have the additional parameters of the electrode finger widths and spacings. As seen from the above discussion, the finger spacing is the parameter which largely determines the response speed, influenced to a degree by the absorption layer thickness, while the absorption layer thickness and the finger spacing–finger width ratio determine the quantum efficiency. The area of the detector is almost irrelevant as only very large devices or ones with closely spaced fingers will have a capacitance large enough to limit the bandwidth, and the large area makes high efficiency fiber-coupling simple.

In Fig. 23 we plot the 3 dB bandwidths computed for "1 × 1," "1 × 2," and "1 × 3" detectors against their external quantum efficiency for 1.55 μm front illumination. The detectors are assumed AR coated. The solid lines are for devices with 1 μm electrodes and the dashed lines are for 0.5 μm wide fingers, assuming that the change in the bandwidth is negligible.

It is clear from Fig. 23 that in order to attain the highest bandwidths both a narrow spacing and a thin absorption layer are required. However, both these demands (for a constant finger width) reduce the quantum efficiency. A bandwidth of >18 GHz appears attainable in a 1 μm finger detector, but only at a

Authorized licensed use limited to: IEEE Xplore. Downloaded on March 4, 2009 at 03:08 from IEEE Xplore. Restrictions apply.

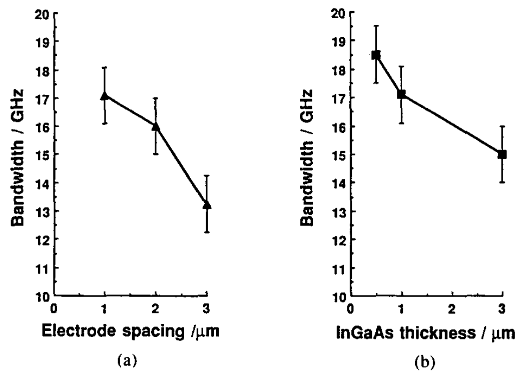

Fig. 22. (a) Bandwidth of the "1 × 1," "1 × 2," and "1 × 3" 1 μm InGaAs detectors examined in Fig. 19(a); (b) bandwidth of the "1 × 1" MSM as a function of InGaAs layer thickness, as examined in Fig. 19(b).

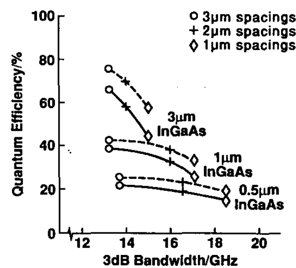

Fig. 23. Trade off between efficiency and bandwidth for the InGaAs MSM. The lines drawn link detectors with the same InGaAs layer thickness 0.5, 1, 2, and 3 μm. The solid lines are for detectors with 1 μm wide fingers, and dashed lines for those with 0.5 μm fingers (assuming no change in the bandwidth). The evaluated points are for detectors with 1, 2, and 3 μm interdigital spacings.

quantum efficiency of <20%. On the other hand, an efficiency of >70% is possible, together with a bandwidth of ~ 12 GHz, if a thick InGaAs layer is used. For this detector, the quantum efficiency is only limited by the fraction of the device area blocked by the electrodes and a significant increase in the efficiency appears possible, at only a moderate cost to the bandwidth, with the use of somewhat narrower fingers and wider electrode spacings. For example, a "0.3 × 4" detector would have a quantum efficiencies of 93% and might be expected to have a bandwidth approaching 10 GHz. The individual requirements of the particular receiver will determine whether a high quantum efficiency or the highest bandwidth is more desirable.

To date, most device results have been reported as pulse response measurements. An evaluation of the associated bandwidth may be made from the pulse response by deconvolving the system response and transforming to the frequency domain. However, we note that this deconvolution must be done numerically, using the system response measured with a very fast characterized detector mounted in a similar fashion to the detector, and the result then numerically Fourier transformed to obtain the frequency response. Simply assuming a Gaussian detector and system response (which, from the typical pulse response, is very clearly quite inappropriate) generally leads to a gross over-estimate of the detector bandwidth.

A numerical deconvolution of the system response for the experimental result in Fig. 20, and for the responses of devices with different finger spacings, indicates experimental bandwidths of 2–4 GHz less than those predicted by the transit-time limited theory. Although these precise figures should be treated with some caution (the system width is 70–80% of the measured response), they do indicate that improvements in device speed are still possible. This will most likely be achieved by grading out the conduction and valence band off sets at the InAlAs-InGaAs interface, as discussed above.

Finally, we note that it is tempting to suggest the use of the electron velocity peak at fields of ~0.2-2 V/μm to obtain a fast pulse response [56]. However, the slower velocity of the holes at these field strengths leads to a very broad hole pulse and will limit the available bandwidth. On the other hand, the use of electron overshoot [51] in "thin" detectors with highly sub-μm finger spacings, where the time of flight is on the scale of the energy relaxation time (~0.2 ps), may be a useful way of increasing the response speed [57].

VIII. Integrating the MSM

As mentioned in the introduction, one of the main driving forces behind the development of the MSM detector is its ease of integration with other components into monolithic receiver circuits. Integration of electronic and optical components to form optoelectronic integrated circuits (OEIC's) and the integration of several optical components together into what has recently been termed "photonic integrated circuits" (PIC's) is expected to produce small-size high performance optoelectronic subsystems which have both high reliability and low unit cost. This was the same motivation that spurred the development of integrated electronics. In the case of OEIC's and PIC's, however, there is the additional formidable challenge of integrating very diverse components, all with different material and processing requirements [58], [59]. Two examples of the sort of integrated multifunctional subsystem envisaged are illustrated in Fig. 24. The components in these two examples range from optical waveguides, waveguide-couplers, and tunable filters, through photodetectors, to transistors and other electronic components. It is a difficult task to integrate these very dissimilar components, especially if they are nonplanar, without compromising the individual performance of each. Great strides are being made, however; for example in the realization of a balanced receiver chip for coherent systems application [60], [61]. It is precisely for these forms of highly complex multifunctional circuits that the MSM detector, with its planar electrodes and simplicity of fabrication, is highly suited. The incorporation of the MSM into an OEIC or PIC would be expected to place minimal design restrictions on the other components in the circuit and the MSM is thus an ideal choice for photodetector. Recently, there has been significant progress made on the integration of the InGaAs MSM with both optical waveguides, on the "up-stream" side, and with transistors to form receiver circuits on the "down-stream" side.

Two InP based waveguide-integrated MSM detectors which have been investigated are shown in Fig. 25 [62]–[65]. In one, the detector sits on top of the guide and light couples up into it from the guided wave passing beneath [62], [63], [65]. In the other, the guided light "butt-couples" into the side of the detector absorption region from the end of the waveguide [64], [65]. In both cases the efficiency of the light detection was high, some 80-90%. A maximum of 100% external efficiency is theoretically possible because the electrodes no longer block any of the incident light. The loss of 10–20% in these cases was

Authorized licensed use limited to: IEEE Xplore. Downloaded on March 4, 2009 at 03:08 from IEEE Xplore. Restrictions apply.

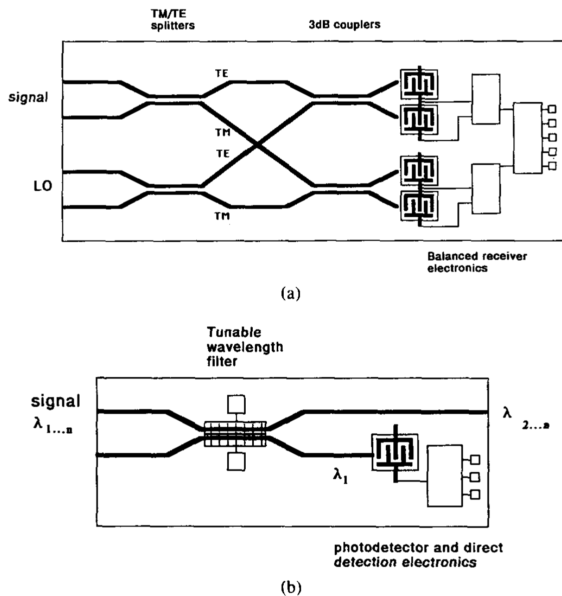

Fig. 24. Two proposed monolithically integrated circuits. (a) A polarization diversity receiver, integrating polarization splitters and local oscillator coupling waveguides with balanced detector receiver circuits. (b) A wavelength selective receiver tap for wavelength multiplexed systems.

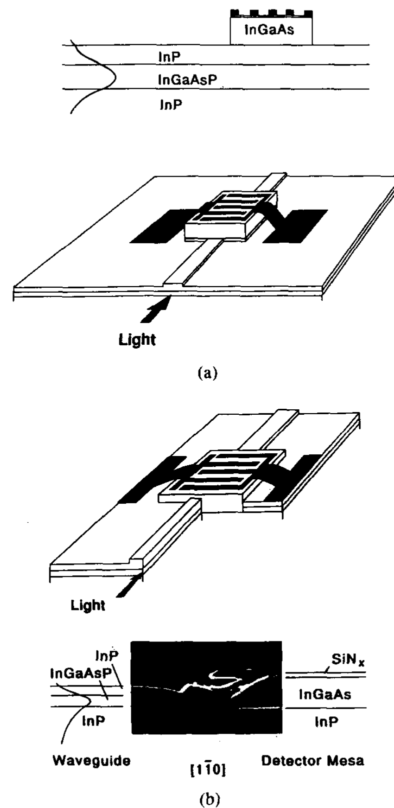

Fig. 25. MSM detector integrated with InP based waveguides: (a) vertical-coupling geometry, where the detector sits on top of the waveguide. This structure involves a single growth. (b) Butt-coupled waveguide detector. Regrowth is required. Also, an SEM micrograph of the cross section through the detector-waveguide interface in such a device. In this case the mesa-etched detector was masked and the waveguide was regrown.

due to ''parasitic'' effects which could be largely eliminated by careful design. There has also been a recent report of an MSM quantum-well waveguide detector grown on GaAs [66], which uses an InGaAs-GaAs strained-layer quantum well to operate at ~ 1.3 μm wavelength.

The ''vertically-coupled'' MSM detector may be designed to absorb only a small fraction of the guided light; in such a configuration it acts as an ''optical tap'' and may be used to monitor the power in the waveguide, or for signal recognition, routing or otherwise processing the guided light signal further down stream. The same geometry may also be used as a terminating detector. In this case, the device might have to be more than a hundred μm long in order to absorb all the guided wave power, and low capacitance of the MSM detector would be of particular advantage as there will be no attendant loss of bandwidth and negligible additional noise.

In the ''butt-coupled'' geometry, all the guided light is absorbed in a few μm length of the InGaAs, almost independent of the waveguide structure. Only a short terminating detector is thus required. This type of detector is necessary when the guide structure is incompatible with vertically-coupled detection; for example where the guided mode must be tightly confined within the guiding core. Regrowth of either the waveguide or the photodetector, or growth on a patterned substrate is required [in [64] and Fig. 25(b) the waveguide was regrown] but this may be combined with the regrowth step often required in receiver fabrication (see below). Indeed, some waveguides require a two-stage growth anyway; e.g., in the case where a polarization insensitive grating coupler is incorporated into a waveguide structure. The resultant planarity of the guide and butt-coupled MSM, with its planar top contacts, facilitates tight dimensional control in the subsequent processing and thus presents a surface structure which is very well suited for further levels of integration.

One disadvantage of the MSM when used as a waveguide detector which must be recognized, however, is that carrier generation now also occurs under the electrodes and, as discussed in the previous section, this leads to a slower pulse response, comparable with that of the back-illuminated discrete device. The reduction in speed, however, may only be relatively modest, especially if sub-μm electrode fingers are used, and calculations indicate that bandwidths of 5-10 GHz should be realizable using a ''conventional'' structure. A bandwidth of 2.7 GHz has already been demonstrated [64], limited in that case by carrier diffusion effects and some carrier pile-up, both of which might be eliminated by careful design. Higher speeds, approaching 10-15 GHz, should be attainable if a thinner absorption layer is used in conjunction with slightly sub-μm electrodes. These bandwidths are also possible in the ''vertically coupled'' scheme, or in a hybrid butt-coupling-vertical-coupling scheme where a thin butt-coupled detector is grown on top of a quasi-guiding layer [65].

On the receiver side, there has been much research reported recently on the integration of InGaAs MSM detectors with FET's to form high performance monolithic receivers [67]-[70]. The most complex circuit reported to date [68] comprised an MSM-HEMT preamplifier, a HEMT cascode amplifier,

Authorized licensed use limited to: IEEE Xplore. Downloaded on March 4, 2009 at 03:08 from IEEE Xplore. Restrictions apply.

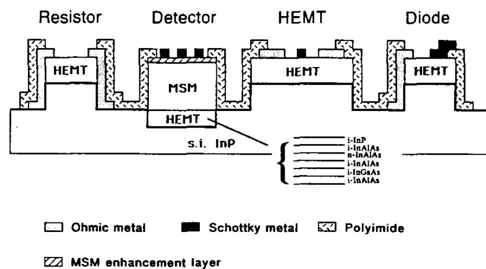

Fig. 26. Diagram of the device structures of the OEIC in [67], which employs growth on a patterned substrate.

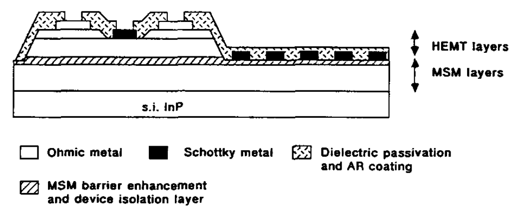

Fig. 27. Device structures in a quasi-planar approach, with the HEMT layers grown on the MSM structure in a single growth on a planar substrate. (After [69]).

Schottky level shifting diodes, and a HEMT output impedance driver—14 components in all—in a transimpedance amplifier formed on a 0.7 mm × 0.6 mm chip. The InAlAs-InGaAs MSM diodes in this circuit were similar to those discussed in the previous sections and the HEMT's employed a conventional modulation doped InAlAs-InGaAs device structure.

Two approaches for MSM-HEMT integration are being followed. In the circuit mentioned above [68] the device layers were grown on a prepatterned substrate. A single growth of the HEMT layers and the MSM layers on top was then followed by removal of the uppermost MSM layers from most of the chip area, which left the detector structure only where there had been a well previously etched in the substrate. The resulting quasi-planar structure was amenable to the fine lithography required in the subsequent processing stages. Ion-milled trenches provided device isolation. A cross section of the resulting structure, showing the MSM, HEMT, and a diode is shown in Fig. 26.

The integrated detectors displayed a low leakage current (~ 1 mA/cm^2 Schottky electrode metal at the operating biases) and the HEMT's had both a high transconductance (260 mS/mm at $V_{gs} = -1$ V) and a high drain saturation current (0.5 A/mm, 1.3 μm wide gates). An amplifier open loop gain of 5.7 was obtained.

In an alternative approach, the HEMT layers are grown on top of the MSM in a single growth on a planar substrate [69], [70]. The resulting structure is illustrated in Fig. 27. The thin (<0.15 μm) HEMT structure maintains a quasi-planar surface and permits fine tolerance lithographic processing of the circuit elements. This considerably simplifies the circuit fabrication procedure.

The two circuits reported to date [69], [70] used the MSM barrier enhancement layer to isolate the HEMT from the MSM, and also for HEMT-HEMT isolation. In [69], a 200 nm Fe-doped InP was used for the barrier enhancement layer (Fe acceptor levels pin the Fermi level at about midgap) and in [70], 150 nm of lattice-matched InAlAs, followed by 200 nm of InAlGaAs grading to InGaAs. In both cases quite low leakage currents of ~ 10 mA/cm^2 were obtained at operating biases, and some gain was recorded at the higher biases. Detector pulse widths were somewhat longer than obtained in the comparable InAlAs-InGaAs detectors considered earlier, probably a consequence of some carrier pileup. In the InP : Fe device there was also apparently significant charge trapping, evidenced by the presence of a pronounced tail. The MBE grown InAlAs-InGaAs MSM-HEMT circuit in [70] comprised an 11 component transimpedance amplifier with 1 μm gate HEMT's (316 mS/mm maximum transconductance, $f_t = 30$ GHz), and gave a clean eye diagram at 2 Gbit/s.

IX. Conclusion

The development of the InGaAs MSM detector has proceeded rapidly over the last couple of years, spurred on by the widely accepted need to realize monolithically integrated receivers operating in the 1.3 and 1.5 μm long wavelength fiber bands. In this paper we have shown how the Schottky barrier MSM offers the unique combination of planarity, simplicity of fabrication, ease of integration, low capacitance and high speed, making it a very good choice for the front end detector in such a receiver.

The capacitance and current characteristic of the MSM have been considered, and the quantum efficiency and speed of the InGaAs MSM at long wavelengths have been discussed in some detail. Practical device results for InAlAs barrier enhanced InGaAs MSMs grown by low pressure OMCVD have been presented. The high performance results which we have illustrated—low leakage, low gain, low noise, and speeds close to the theoretical limits—indicate that the development of this particular device is now sufficiently advanced for it to be integrated into high performance monolithic receivers. Current progress on such integration has been discussed. Whatever the particular technology that finally becomes established for raising the effective Schottky barrier on InGaAs MSM detectors, this barrier-enhancement device promises to be a photodetector of great importance for long wavelength communications.

Acknowledgment

The authors would like to express their thanks to R. Bhat and M. A. Koza for their excellent quality OMCVD material that made their development of the InAlAs-InGaAs MSM photodetector possible. Also, to H. P. LeBlanc for fabrication expertise and technical assistance. Finally, they would like to thank R. F. Leheny for suggesting the writing of this paper, and J. R. Hayes for his support during its completion.

References

[1] M. Makiuchi, H. Hamaguchi, T. Kumai, M. Ito, O. Wada, and T. Sakurai, "A monolithic four-channel photoreceiver integrated on a GaAs substrate using metal-semiconductor-metal photodiodes and FETs," *IEEE Electron Devices Lett.*, vol. EDL-6, pp. 634–635, 1985.

[2] W. S. Lee, G. R. Adams, J. Mun, and J. Smith, "Monolithic GaAs photoreceiver for high-speed signal processing applications," *Electron. Lett.*, vol. 22, pp. 147–148, 1986.

[3] C. S. Harder, B. J. Van Zeghbroeck, H. Meier, W. Patrick, and P. Vettiger, "5.2 GHz bandwidth monolithic GaAs optoelectronic receiver," *IEEE Electron Devices Lett.*, vol. 9, pp. 171–173, 1988.

[4] J. D. Crow, C. J. Anderson, S. Bermon, A. Callegari, J. F. Ewen, J. D. Feder, J. H. Greiner, E. P. Harris, P. D. Hoh, H. J. Hovel, J. H. Magerlein, T. E. Mckoy, A. T. S. Pomerene, D. L. Rogers, G. J. Scott, M. Thomas, G. W. Mulvey, B. K. Ko,

Authorized licensed use limited to: IEEE Xplore. Downloaded on March 4, 2009 at 03:08 from IEEE Xplore. Restrictions apply.

T. Ohashi, M. Scontras, and D. Widiger, "A GaAs MESFET IC for optical multiprocessor networks," *IEEE Trans. Electron Devices*, vol. 36, pp. 263-268, 1989.

[5] S. D. Personick, *Optical Fiber Transmission Systems*, New York: Plenum, 1981.

[6] R. G. Smith and S. D. Personick, "Receiver design for optical fiber communications systems," in *Semiconductor Devices for Optical Communications*, H. Kressel, Ed., New York: Springer-Verlag, 1980.

[7] L. Figuera and C. W. Slayman, "A novel heterostructure interdigitated photodetector (HIP) with picosecond optical response," *IEEE Trans. Electron Devices*, vol. ED-2, pp. 208-210, 1981.

[8] M. Ito and O. Wada, "Low dark current GaAs metal-semiconductor-metal (MSM) photodiodes using WSi_x contacts," *IEEE J. Quantum Electron.*, vol. QE-22, pp. 1073-1077, 1986.

[9] W. Roth, H. Schumacher, J. Kluge, H. Geelen, and H. Beneking, "The DSI diode-A fast large area optoelectronic detector," *IEEE Trans. Electron Devices*, vol. ED-2, pp. 1034-1036, 1985.

[10] K. Kajiyama, Y. Mizushima, and S. Sakata, "Schottky barrier height of n^--InGaAs diodes," *Appl. Phys. Lett.*, vol. 23, pp. 458-460, 1973.

[11] H. Schumacher, H. P. LeBlanc, J. Soole, and R. Bhat, "An investigation of the optoelectronic response of GaAs/InGaAs MSM photodetectors," *IEEE Electron Devices Lett.*, vol. 9, pp. 607-609, 1988.

[12] T. Kikuchi, H. Ohno, and H. Hasegawa, "$In_{0.53}Ga_{0.47}As$ metal-semiconductor-metal photodiodes using a lattice mismatched AlGaAs Schottky assist layer," *Electron. Lett.*, vol. 24, pp. 1208-1210, 1988.

[13] W.-P. Hong, G.-K. Chang, and R. Bhat, "High performance $Al_{0.15}Ga_{0.85}As/In_{0.53}Ga_{0.47}As$ MSM photodetectors grown by OMCVD," *IEEE Trans. Electron. Devices*, vol. 4, pp. 659-662, 1988.

[14] W. K. Chan, G.-K. Chang, R. Bhat, N. E. Schlotter, and C. K. Nguyen, "High-speed GaInAs MISIM photodetectors with dielectric-assisted Schottky barriers," *IEEE Electron Devices Lett.*, vol. 10, pp. 417-419, 1989.

[15] L. Yang, A. S. Sudbo, R. A. Logan, T. Tanbun-Ek, and W. T. Tsang, "High performance of Fe:InP/InGaAs metal/semiconductor/metal photodetectors grown by vapor phase epitaxy," *IEEE Photon. Technol. Lett.*, vol. 2, pp. 56-58, 1990.

[16] J. B. D. Soole, H. Schumacher, H. P. LeBlanc, R. Bhat, and M. A. Koza, "High-speed performance of OMCVD grown InAlAs/InGaAs MSM photodetectors at 1.5 μm and 1.3 μm wavelengths," *IEEE Photon. Technol. Lett.*, vol. 1, pp. 250-252, 1989.

[17] O. Wada, H. Nobuhara, H. Hamguchi, T. Mikawa, A. Tackeuchi, and T. Fujii, "Very high speed GaInAs metal-semiconductor-metal photodiode incorporating an AlInAs/GaInAs graded superlattice," *Appl. Phys. Lett.*, vol. 54, pp. 16-17, 1989.

[18] J. B. D. Soole, H. Schumacher, H. P. LeBlanc, R. Bhat, and M. A. Koza, "High frequency performance of InGaAs metal-semiconductor-metal photodetectors at 1.55 and 1.3 μm wavelengths," *Appl. Phys. Lett.*, vol. 55, pp. 729-731, 1989.

[19] ——, "High performance $In_{0.52}Al_{0.48}As/In_{0.53}Ga_{0.47}As$ metal-semiconductor-metal photodetectors," in *Conf. Proc.*, IEDM, Washington, DC, paper 30.1, pp. 713-716, 1989.

[20] G.-K. Chang, W.-P. Hong, J. L. Gimlett, R. Bhat, and C. K. Nguyen, "High performance monolithic dual-MSM photodetector for long wavelength coherent receivers," *Electron. Lett.*, vol. 25, pp. 1021-1022, 1989.

[21] D. H. Lee, S. L. Sheng, N. J. Sauer, and T. Y. Chang, "High quality $In_{0.53}Ga_{0.47}As$ Schottky diode formed by graded superlattice of $In_{0.53}Ga_{0.47}As/In_{0.52}Al_{0.48}As$," *Appl. Phys. Lett.*, vol. 19, pp. 1863-1866, 1989.

[22] H. T. Griem, S. Ray, J. L. Freeman, and D. L. West, "Long-wavelength (1.0-1.6 μm) $In_{0.52}Al_{0.48}As/In_{0.53}(Ga_xAl_{1-x})_{0.47}As/In_{0.53}Ga_{0.47}As$ metal-semiconductor-metal photodetector," *Appl. Phys. Lett.*, vol. 56, pp. 1067-1068, 1990.

[23] C. L. Lin, P. Chu, A. L. Kellner, H. H. Wieder, and E. A. Rezek, "Compositional dependence of $Au/In_xAl_{1-x}As$ Schottky barrier heights," *Appl. Phys. Lett.*, vol. 49, pp. 1593-1595, 1986.

[24] D. Rogers, J. M. Woodall, G. D. Pettit, and D. McInturff, "High-speed 1.3 μm GaInAs detectors fabricated on GaAs substrates," *IEEE Electron Devices Lett.*, vol. 9, pp. 515-517, 1988.

[25] M. Zirngibl, J. C. Bischoff, D. Theron, and M. Ilegems, "A superlattice GaAs/InGaAs-on-GaAs photodetector for 1.3 μm applications," *IEEE Electron Devices Lett.*, vol. 10, pp. 336-338, 1989.

[26] Y. C. Lim and R. A. Moore, "Properties of alternately charged coplanar parallel strips by conformal mappings," *IEEE Trans. Electron Devices*, vol. ED-15, pp. 173-180, 1968.

[27] S. M. Sze, D. J. Coleman Jr., and A. Loya, "Current transport in metal-semiconductor-metal (MSM) structures," *Solid-State Electron.*, vol. 14, pp. 1209-1218, 1971.

[28] Ch. S. Harder, B. J. Van Zeghbroeck, M. P. Kessler, H. P. Meier, P. Vettiger, D. J. Webb, and P. Wolf, "High speed GaAs/AlGaAs optoelectronic devices for computer applications," *IBM J. Res. Develop.*, vol. 34, pp. 568-584, 1990.

[29] S. M. Sze, *Physics of semiconductor devices*, 2nd Ed., New York: Wiley, 1981.

[30] C. K. Peng, A. Ketterson, H. Morkoç, and P. M. Solomon, "Determination of the conduction-band discontinuity between $In_{0.53}Ga_{0.47}As/In_{0.52}Al_{0.48}As$ using n^+-InGaAs/InAlAs/n^--InGaAs capacitors," *J. Appl. Phys.*, vol. 60, pp. 1709-1711, 1986.

[31] G.-K. Chang, private communication.

[32] J. B. D. Soole, unpublished.

[33] D. A. Humphreys, R. J. King, D. Jenkins, and A. J. Moseley, "Measurement of absorption coefficients of $Ga_{0.47}In_{0.53}As$ over the wavelength range 1.0-1.7 μm," *Electron. Lett.*, vol. 21, pp. 1187-1188, 1985.

[34] D. L. Rogers, J. M. Woodall, G. D. Pettit, and D. McIntuff, "High-speed 1.3 μm GaInAs detectors fabricated on GaAs substrates," *IEEE Electron Devices Lett.*, vol. 9, pp. 515-517, 1988.

[35] S. R. Forrest, O. K. Kim, and R. G. Smith, "Optical response time of $In_{0.52}Al_{0.48}As/InP$ avalanche photodiodes," *Appl. Phys. Lett.*, vol. 41, pp. 95-97, 1982.

[36] J. E. Bowers and C. A. Burrus, "High-speed zero bias waveguide photodetectors," *Electron. Lett.*, vol. 22, pp. 905-906, 1986.

[37] J. B. D. Soole, H. P. Hughes, and N. Apsley, "Electromagnetic resonance enhanced photoabsorption in planar metal-oxide-metal tunnel junction photodetectors," *J. Appl. Phys.*, vol. 61, pp. 2022-2029, 1987.

[38] R. W. Rendell and D. J. Scalapino, "Surface plasmons confined by microstructures on tunnel junctions," *Phys. Rev. B*, vol. 24, pp. 3276-3294, 1981.

[39] J. B. D. Soole, R. N. Lamb, H. P. Hughes, and N. Apsley, "Surface plasmon enhanced photoconductivity in planar metal-oxide-metal tunnel junctions," *Solid State Commun.*, vol. 9, p. 607, 1986.

[40] W. C. Koscielniak, R. M. Kolbas, M. A. Littlejohn, and B. W. Liczerski, "Photocurrent enhancement in a GaAs metal-semiconductor-metal photodetector due to ultrasmall Au islands," *Appl. Phys. Lett.*, vol. 52, pp. 987-989, 1988.

[41] W. C. Koscielniak, R. M. Kolbas, and M. A. Littlejohn, "Performance of a near-infrared GaAs metal-semiconductor-metal (MSM) photodetector with islands," *IEEE Electron Devices Lett.*, vol. 9, pp. 485-486, 1990.

[42] T. V. Muoi, "Receiver design for high-speed optical-fiber systems," *J. Lightwave Technol.*, vol. LT-2, pp. 243-267, 1984.

[43] G. Sasaki, W. P. Hong, G.-K. Chang, R. Bhat, F. S. Turco, and H. P. LeBlanc, "Low-frequency noise characteristics of AlInAs/GaInAs modulation-doped field-effect transistors," *Electron. Lett.*, vol. 25, pp. 1039-1040, 1989.

[44] C.-Y. Su, H. Rohdin, and C. Stolte, "1/f noise in GaAs MESFETs," in *Conf. Proc.*, IEDM, Washington, DC, paper 27.2, pp. 601-604, 1983.

[45] O. Wada, H. Hamaguchi, L. Le Beller, and C. Y. Boisrobert, "Noise characteristics of GaAs metal-semiconductor-metal photodiodes," *Electron. Lett.*, vol. 24, pp. 1574-1575, 1988.

[46] H. Schumacher, J. B. D. Soole, H. P. LeBlanc, R. Bhat, and M. A. Koza, "Noise behaviour of InAlAs/InGaAs MSM photodetectors," *Electron. Lett.*, vol. 26, pp. 612-614, 1990.

[47] J. E. Bowers and C. A. Burrus, "Ultra-wide-band long-wavelength PIN photodetectors," *J. Lightwave Technol.*, vol. LT-5, pp. 1339-1350, 1987.

[48] J. E. Bowers, C. A. Burrus, and R. J. McCoy, "InGaAs pin photodiodes with modulation response to millimetre wavelengths," *Electron. Lett.*, vol. 21, pp. 812-814, 1985.

[49] W. C. Koscielniak, J. L. Pelouard, and M. A. Littlejohn, "Dynamic behaviour of photocarriers in a GaAs metal-semiconduc-

Authorized licensed use limited to: IEEE Xplore. Downloaded on March 4, 2009 at 03:08 from IEEE Xplore. Restrictions apply.

tor-metal photodetector with sub-half-micron electrode pattern," *Appl. Phys. Lett.*, vol. 54, pp. 567-569, 1989.
[50] J. B. D. Soole and H. Schumacher, "Transit-time limited frequency response of InGaAs M-S-M photodetectors," *IEEE Trans. Electron Devices*, vol. 37, pp. 2285-2291, 1990.
[51] J. G. Ruch, "Electron dynamics in short channel field-effect transistors," *IEEE Trans. Electron Devices*, vol. ED-19, pp. 652-654, 1972.
[52] A. Yariv, *Optical Electronics*, 3rd Ed., New York: Holt, Rinehart and Winston, 1985.
[53] T. H. Wood, J. Z. Pastalan, C. A. Burrus, B. I. Miller, J. L. deMiguel, U. Koren, and M. Young, "Electroabsrption in GaAs/InP multiple quantum wells at high optical intensities," presented at Integrat. Photon. Res. Conf., Hilton Head SC, Mar. 1990, paper TuG4.
[54] M. Suzuki, H. Tanaka, and S. Akiba, "Effect of hole pile-up at hetero-interface on modulation voltage in GaInAsP electroabsorption modulators," *Electron. Lett.*, vol. 25, pp. 88-89, 1990.
[55] C. Jagannath, A. N. M. M. Choudhury, B. Elman, and C. A. Armiento, "1.3 μm InGaAs/GaAs interdigitated metal-semiconductor-metal photodetectors," presented at Integrat. Photon. Res. Conf., Hilton Head, SC, Mar. 1990, paper TuA7.
[56] M. Smiljanic, Z. Djuric, and Z. Lazic, "Electron transit-time through depletion layer of GaInAs pn junction," *Electron. Lett.*, vol. 25, pp. 151-152, 1989.
[57] A. Cappy, B. Carnez, R. Fauquembergues, G. Salmer, and E. Constant, "Comparative potential performance of Si, GaAs, GaInAs submicrometer-gate FETs," *IEEE Trans. Electron. Devices*, vol. ED-27, pp. 2158-2160, 1980.
[58] O. Wada, T. Sakurai, and T. Nakagami, "Recent progress in optoelectronic integrated circuits (OEIC's)," *IEEE J. Quantum Electron.*, vol. 6, pp. 805-821, 1986.
[59] M. Dagenais, R. F. Leheny, H. Temkin, and P. Bhattacharya, "Applications and challanges of OEIC Technology: a report on the 1989 Hilton Head Workshop," *J. Lightwave Technol.*, vol. 8, pp. 846-862, 1990.
[60] T. L. Koch, U. Koren, R. P. Gnall, F. S. Choa, F. Hernandez-Gil, C. A. Burrus, M. G. Young, M. Oron, and B. I. Miller, "GaInAs/GaInAsP multiple quantum-well integrated heterodyne receiver," *Electron. Lett.*, vol. 25, pp. 1621-1623, 1989.
[61] H. Takeuchi, K. Kasaya, Y. Kondo, H. Yasaka, K. Oe, and Y. Imamura, "Monolithic integrated coherent receiver on InP substrate," *IEEE Photon. Technol. Lett.*, vol. 1, pp. 398-400, 1989.
[62] J. B. D. Soole, H. Schumacher, R. Esagui, M. A. Koza, and R. Bhat, "Waveguide integrated MSM photodetector on InP," *Electron. Lett.*, vol. 24, pp. 1478-1480, 1988.
[63] J. B. D. Soole, H. Schumacher, R. Esagui, H. P. LeBlanc, R. Bhat, and M. A. Koza, "High speed metal-semiconductor-metal waveguide photodetector on InP," *Appl. Phys. Lett.*, vol. 55, pp. 2173-2175, 1989.
[64] J. B. D. Soole, H. Schumacher, H. P. LeBlanc, R. Bhat, and M. A. Koza, "Butt-coupled InGaAs metal-semiconductor-metal waveguide photodetector formed by selective area regrowth," *Appl. Phys. Lett.*, vol. 56, pp. 1518-1520, 1989.
[65] —, "Waveguide integrated metal-semiconductor-metal photodetectors for long wavelength applications," presented at IEEE/LEOS Top. Meet. Optoelectron., Monterey, CA, July 1990, paper IOT10.
[66] C. Jagannath, A. Silletti, A. N. M. M. Choudhury, B. Elman, and P. Melman, "1.3 μm monolithically integrated waveguide-interdigitated metal-semiconductor-metal photodetector on a GaAs substrate," *Appl. Phys. Lett.*, vol. 56, pp. 1892-1894, 1990.
[67] W.-P. Hong, G.-K. Chang, R. Bhat, J. L. Gimlett, C. K. Nguyen, G. Sasaki, and M. Koza, "High performance $In_{0.52}Al_{0.48}As/In_{0.53}Ga_{0.47}As$ MSM-HEMT receiver OEIC grown by MOCVD on patterned InP substrates," *Electron. Lett.*, vol. 25, pp. 1561-1563, 1989.
[68] G.-K. Chang, W. P. Hong, J. L. Gimlett, R. Bhat, C. K. Nguyen, G. Saski, and J. C. Young, "A 3 GHz transimpedance OEIC receiver for 1.3-1.5 μm fiber optic systems," *IEEE Photon. Technol. Lett.*, vol. 2, pp. 197-199, 1990.
[69] L. Yang, A. S. Sudbo, W. T. Tsang, P. A. Garbinski, and R. M Camarda, "Monolithic integrated InGaAs-InP MSM-FET photoreceiver prepared by chemical beam epitaxy," *IEEE Photon. Technol. Lett.*, vol. 2, pp. 59-61, 1990.
[70] H. T. Griem, H. S. Fuji, T. J. Williams, J. P. Harring, R. R. Daniels, S. Ray, M. J. LaGasse, and D. L. West, "Monolithically integrated InGaAs/InAlAs (on InP) MSM/FET photoreceiver by MBE," presented at Device Res. Conf., Santa Barbara, CA June 1990, paper 111B-6.

Julian B. D. Soole received the B.A. degree in natural sciences in 1982 and the M.A. degree in 1986 from the University of Cambridge, England. He received the Ph.D. degree from the University of Cambridge in 1988. His research included surface plasmon effects in planar metal-oxide-metal tunnel junctions, and was conducted at the Cavendish Laboratory.

In 1988 he joined Bellcore, Red Bank, NJ, where he is a member of the technical staff in the high speed device research district. His research work is in the area of high speed optoelectronics, with current primary focus on III-V based waveguide devices and integrated optoelectronic components.

Hermann Schumacher was born in Siegen, West Germany, on May 5, 1957. He received the Dipl.-Ing. degree in electrical engineering from Aachen University of Technology, Aachen, West Germany, in 1982 and the Dr.-Ing. degree (with honors) in 1986, also from Aachen University, for work on picosecond optoelectronic sampling systems used to characterize high speed planar photodetectors on GaAs and InGaAs.

In 1986, he joined Bellcore, Red Bank, NJ, as a member of the technical staff in the high-speed device research district where he worked on the design, fabrication, and characterization of high speed optoelectronic and electronic devices including photodetectors and heterojunction bipolar transistors. In September 1990, he joined the University of Ulm, Ulm, Germany, as an associate professor in the Department of Electronic Devices and Circuits.

Authorized licensed use limited to: IEEE Xplore. Downloaded on March 4, 2009 at 03:08 from IEEE Xplore. Restrictions apply.